ACS Catalysis
Research Article
pubs.acs.org/acscatalysis

Insights into Heterogeneous Catalysis of Persulfate Activation on Dimensional-Structured Nanocarbons

Xiaoguang Duan, Hongqi Sun,* Jian Kang, Yuxian Wang, Stacey Indrawirawan, and Shaobin Wang*

Department of Chemical Engineering, Curtin University, GPO Box U1987, WA6845 Perth, Australia

S *Supporting Information*

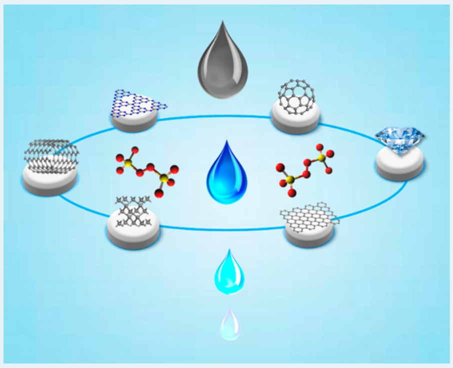

ABSTRACT: A variety of dimensional-structured nanocarbons were applied for the first time as metal-free catalysts to activate persulfate (PS) for catalytic oxidation of phenolics and dyes as well as their degradation intermediates. Single-walled carbon nanotubes (SWCNTs), reduced graphene oxide (rGO), and mesoporous carbon (CMK-8) demonstrated superior catalytic activities for heterogeneous PS activation, whereas fullerene (C_{60}), nanodiamonds, and graphitic carbon nitride (g-C_3N_4) presented low efficiencies. Moreover, the carbocatalysts presented even better catalytic performances than activated carbon and metal oxides, such as Fe_3O_4, CuO, Co_3O_4, and MnO_2. The activity of prepared rGO-900 was further competing to the most efficient electron donor of zerovalent iron (ZVI). Both characterization and oxidation results suggested that the catalytic performances of the nanocarbons are determined by the intrinsic atom arrangements of carbon hybridization, pore structure, defective sites, and functional groups (especially the carbonyl groups). Electron paramagnetic resonance (EPR) spectra revealed that carbocatalysts might act as an excellent electron bridge in activation of PS to oxidize adsorbed water directly to generate hydroxyl radicals, distinct from homogeneous and metal-based catalytic activation. This study discovers several efficient nanocarbons for heterogeneous PS activation, and it presents new insights into the catalytic activation processes, providing a fascinating strategy to develop metal-free catalysts for green remediation.

KEYWORDS: *carbocatalysis, persulfate, metal-free, heterogeneous, EPR*

INTRODUCTION

In recent decades, environmental deterioration issues such as sandy desertification, air pollution, and soil and water contamination have interrupted the balance of harmonious coexistence between nature and human beings. The excessive hazardous compounds in industrial wastewater and domestic sewage have been far beyond the natural degradation capability by the ecosystem. Therefore, state-of-the-art remediation technologies for adsorption and catalytic oxidation of aqueous pollutants have been intensively investigated.[1,2] Adsorption presents great performance for phase separation, the adsorbed pollutants are not completely destroyed, and the subsequent disposal or regeneration of adsorbents will likely give rise to secondary contamination.[3] On the other hand, advanced oxidation processes (AOPs), utilizing oxidants such as oxygen, ozone, and superoxides such as H_2O_2, HSO_5^- and $S_2O_8^{2-}$, are able to completely decompose organics into harmless substances, water and carbon dioxide.[3] Conventional Fenton reaction applies ferrous ions to stimulate H_2O_2 to generate hydroxyl radials for AOPs. However, the Fenton process suffers from drawbacks, such as strict pH requirements (~3) and production of large amounts of sludge. Meanwhile, it releases metal ions into the water body, making it both cost-ineffective and noneco-friendly for industrial application. Compared to liquid H_2O_2, persulfate (PS), a white crystal solid, is cheaper (\$0.74/kg vs \$1.5/kg of H_2O_2), more chemically stable, and more convenient to transport, store, and use in various applications, and therefore, there is broad interest in PS for pollutant removal.[4,5]

PS itself presents a low oxidative potential for decomposition of organic compounds without activation processes. The bond distance and energy of O−O (SO_4−SO_4) bonding were estimated to be 1.497 Å and 140 kJ/mol, respectively.[6,7] The symmetric structure of PS molecules and relative high bonding energy make it more difficult to break the O−O bond and generate free radicals without external activation. Various approaches were then applied to activate PS either to generate free radicals such as sulfate ($SO_4^{\bullet-}$) and hydroxyl radicals ($^{\bullet}OH$) or to induce nonradical process to conduct the oxidation processes.[5] Physical activation such as UV irradiation or heating is able to effectively stimulate PS to produce sulfate radicals for oxidation of pollutants.[8−10] Chemical activation such as bases, phenols, and quinones were reported to be effective for activating PS for *in situ* chemical oxidation (ISCO).[11−13] Recent studies also applied electrochemical methods or electron donors (zerovalent iron or ferrous ion (II)) for PS activation.[14−17] Andrew et al. reported that silver(I) was active in catalytic activation of PS for oxidative

Received: April 14, 2015
Revised: June 4, 2015
Published: June 26, 2015

DOI: 10.1021/acscatal.5b00774
ACS Catal. 2015, 5, 4629−4636

decarboxylation of acids, and copper(II) could effectively enhance the catalytic reaction with cocatalysis.[18] All the above approaches require energy or chemical inputs, or discharge toxic substances into the water. However, effective heterogeneous PS activation has been less explored. Zhang and co-workers reported that copper oxide (CuO) can work as an efficient catalyst for PS activation under mild conditions via a nonradical process for oxidative degradation of 2,4-dichlorophenol (2,4-DCP).[5] PS tends to first interact with the outer sphere of CuO, which is supposed to be the rate-limiting step, and then quickly reacts with the target organic pollutants.

We first discovered that chemically reduced graphene oxide (rGO) can work as an effective metal-free catalyst to activate peroxymonosulfate (PMS) to generate reactive radicals.[19] More recently, multiwalled carbon nanotubes (MWCNTs) further demonstrated superior performance for PS activation toward phenol oxidation.[20,21] The sp^2 covalent carbon network and oxygen functional groups (CNT-C═O) at the defective edges of MWCNTs were suggested to conduct a redox cycle for electron transfer to PS to produce radicals, yet insight into mechanistic study of carbocatalysis for PS activation is still lacking. It was reported that nanocarbons with different structure dimensions presented unique properties in charge transportation, electronic conductivity, mechanical strength, and porosity in supercapacitor electrodes.[22,23] However, to the best of our knowledge, the effect of molecular dimensions of nanocarbons on heterogeneous catalysis has rarely been investigated. In this study, a wide variety of carbon allotropes in differently molecular dimensions, such as 0D fullerene and nanodiamonds, 1D SWCNTs and MWCNTs, 2D graphene and g-C_3N_4, and 3D CMK-8, were employed for PS activation for catalytic phenol oxidation. Activated carbon, iron powders and several classical metal oxides were utilized as reference materials. Electron paramagnetic resonance (EPR) was applied as a powerful *in situ* characterization technique to facilitate the first insight into PS activation and radical evolution processes on nanocarbons.

■ RESULTS AND DISCUSSION

The physicochemical properties of carbonaceous materials are displayed in Table 1. Most of the nanocarbons possessed high specific surface areas (SSAs) from 200 to 1000 m^2/g and pore volume at a range of 0.74−1.64 cm^3/g. CMK-8 presented extremely large surface area (1072 m^2/g) and pore volume (1.6 cm^3/g) owing to the cubic-ordered mesoporous structure. However, the SSAs of C_{60} and g-C_3N_4 were only about 4.8 and 11.7 m^2/g, respectively, probably due to the aggregated particles and stacking layers. Figure S1 illustrates that the pore structure of nanocarbons was primarily at the mesoporous region (2−50 nm).

Table 1. Structure and Surface Chemistry of Various Nanocarbons

	SSAs (m^2/g)	pore volume (cm^3/g)	pore size (nm)	Raman I_D/I_G ratio	oxygen content
C_{60}	4.8	0.003	4.2	-	9.1%
SWCNTs	385.2	0.90	8.2	0.46	1.6%
MWCNTs	253.6	0.74	11.2	0.65	2.1%
g-C_3N_4	11.7	0.04	9.5	-	1.1%
rGO-900	462.2	1.00	5.7	1.70	6.0%
nanodiamond	315.5	0.96	8.4	-	4.1%
CMK-8	1071.9	1.64	5.1	1.49	8.8%

The I_D/I_G ratios (defective to graphitic degree) of Raman spectra are widely employed to evaluate the crystalline structure of carbon materials. RGO-900 has a much higher I_D/I_G value (1.70) than that of SWCNTs (0.46) and MWCNTs (0.65), due to the reconstruction of carbon network and the creation of defective sites during the synthesis process. XPS study was performed to investigate the surface chemistry and chemical states of elements in the catalysts (Figure S2). It is well-known that the edges of graphene and carbon nanotubes are terminated with hydrogen and oxygen atoms.[24] Most of nanocarbons contained certain amounts of oxygen groups such as hydroxyl (C−OH), carbonyl (C═O), and carboxyl (−COOH) groups, as indicated in Figure S3. The relative high oxygen contents of C_{60} (9.1%) might be ascribed to the adsorbed oxygen molecules and organic compounds from the synthesis process. After thermal treatment, most of the oxygen groups were removed from the surface of GO, and the oxygen level was reduced from 32.0% to 6.0%.

Control experiments of physical activation of PS and phenol adsorption on various nanocarbons were carried out. As shown in Figure 1, PS can hardly oxidize phenol without activation. Only 3.8% of phenol was degraded without the presence of a solid catalyst. Physical strategies such as ultraviolet light radiation and thermal activation (70 °C) provided 18.0% and 23.1% phenol removal accordingly. Phenol adsorption on various nanocarbons was tested as indicated in Figure S4 (Supporting Information, SI). Phenol removal efficiencies of C_{60}, SWCNTs, rGO-900, and CMK-8 were 3.5%, 19.6%, 21.3%, and 35.1%, respectively. It was suggested that the adsorption capacity of nanocarbons is closely related to the structure of nanocarbons, which follows an order: 0D < 1D ∼ 2D < 3D. The nanocarbons with a higher molecular dimension possess more porous structures and larger specific surface areas, giving rising to higher phenol adsorption. Additionally, the versatile oxygen groups on the surface of carbon materials also played crucial roles to enhance the adsorption.

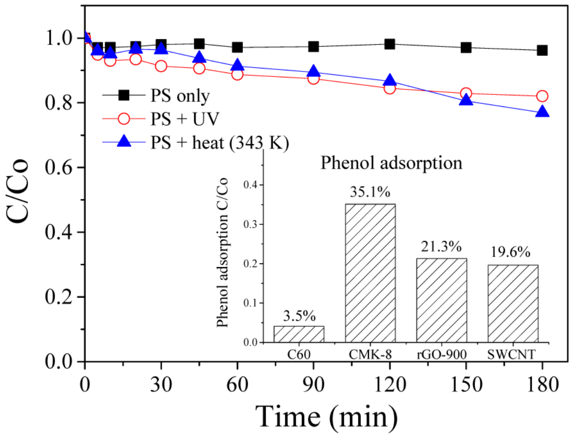

Figure 1. Phenol adsorption and PS activation under various conditions. [Catalyst] = 0.2 g/L; [Temp] = 25 °C; [PS] = 6.5 mM; [Phenol] = 20 ppm.

The catalytic activities of various nanocarbons toward PS activation were evaluated for phenol oxidation. Figure 2 shows that PS could barely be activated by C_{60} and g-C_3N_4, producing only 3.8% and 4.0% phenol removal efficiencies, respectively.

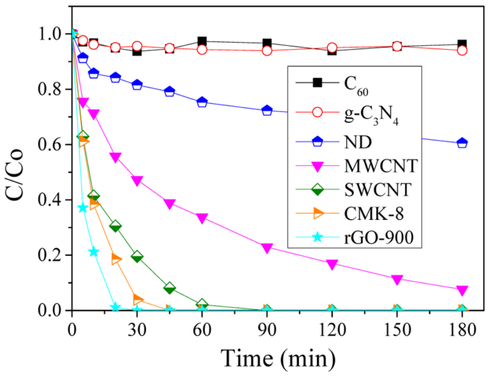

Figure 2. Phenol oxidative degradation on various nanocarbons. [Catalyst] = 0.2 g/L; [Temp] = 25 °C; [PS] = 6.5 mM; [Phenol] = 20 ppm.

Around 39.5% and 92.5% of phenol was decomposed in 180 min on pristine nanodiamond and MWCNTs. It was found that SWCNTs, CMK-8, and rGO-900 presented outstanding performances for PS activation, providing complete phenol degradation in 90, 45, and 30 min, accordingly. The reaction intermediates during the phenol oxidation were investigated and illustrated in Figure 3 and Figure S5 (SI) to reveal the phenol degradation pathways. Several standard compounds were utilized to identify the intermediates, as shown in Figure S6 (SI). It can be suggested that phenol was first oxidized to 1,2-hydrobenzene and benzoquinone, and subsequently, the benzene ring was opened and oxidized to small molecular acids such as malonic acid, malic acid, and formic acid. Figure 4 further demonstrated that the nanocarbons presented great efficiency for catalytic oxidation of other organic pollutants such as methylene blue (MB), 2,4-DCP, catechol, and 1,4-dihydroxybenzene, among others.

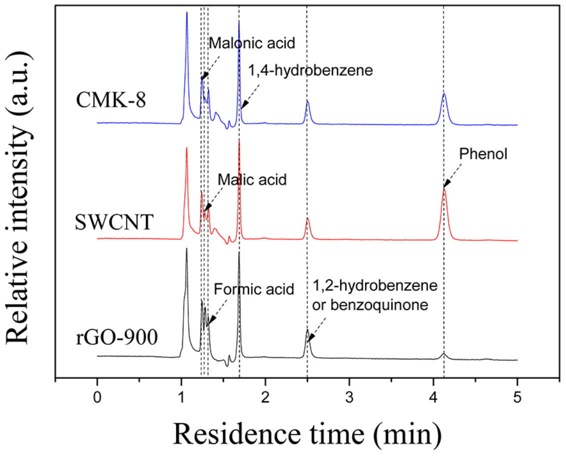

Figure 3. Intermediates detection in phenol oxidation on nanocarbons. [Temp] = 25 °C; [PS] = 6.5 mM; [Phenol] = 20 ppm; [Carbocatalyst] = 0.2 g/L, [Reaction time] = 30 min.

During synthesis of nanocarbons, metal impurities are always unavoidably introduced into the carbon materials in spite of physical and chemical post-treatments such as mechanical separation and acid washing.[25,26] It is well reported that trace metal residues might significantly influence the carbocatalyst-based heterogeneous reactions.[25,27−29] However, in this study, Figure S2 (SI) confirmed that no significant metal elements were found in the XPS spectra of the nanocarbons. The effect of metal residues was further ruled out by employing the ash of nanocarbons as catalysts for phenol oxidation. Figure S7 (SI) suggests that the ash presented poor activity for PS activation. Furthermore, the digested solutions of carbocatalysts after acid washing were employed for PS activation. The experimental results in Figure S8 (SI) further exclude the influence of metal residuals. Herein, the outstanding catalytic activity was exclusively proven to derive from functional groups and active sites of nanocarbons in carbocatalysis for PS activation.

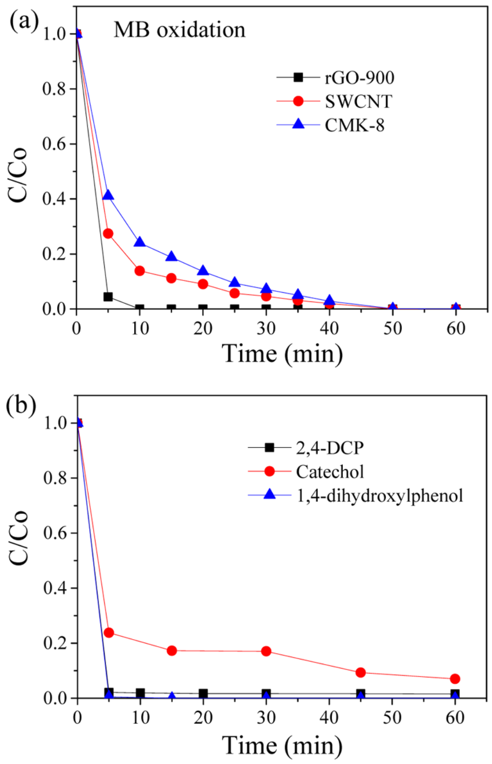

Figure 4. (a) Persulfate activation on nanocarbons for methylene blue degradation ([MB] = 10 ppm); (b) 2,4-DCP, catechol, 1,4-dihydroxybenzene oxidative degradation on rGO-900. ([2,4-DCP] = 10 ppm; [Catechol] or [1,4-dihydroxybenzene] = 20 ppm) [Temp] = 25 °C; [PS] = 6.5 mM; [Carbocatalyst] = 0.2 g/L.

Effect of reaction temperature on catalytic phenol oxidation over nanocarbons by PS activation was further investigated and shown in Figure S9 (SI). The catalytic performances of the nanocarbons in PS activation were improved with elevated temperatures. In general, elevated temperature would promote phenol adsorption and electron transfer from carbon materials to PS to produce reactive radicals, thereby enhancing the phenol degradation.

Su and co-workers reported that improved catalytic activity for aerobic oxidation originated from the synergistic performance of the carboxylic groups and unconfined π electrons at the defective edges of graphene oxide (GO).[30] Frank et al. discovered that the ketonic and quinonic groups (C═O) at the edge of carbon nanotubes were rich in electrons and could work as Lewis basic sites for selectively oxidative dehydrogenation (ODH) of light alkanes to alkenes.[31,32] In environmental remediation, we first reported that rGO prepared by a hydrothermal method demonstrated an excellent activity to activate peroxymonosulfate (PMS) for organic pollutant oxidation.[19] The surface acidity of GO was tuned by removal of oxygen groups with ammonia solution. The minor oxygen groups, especially the carbonyl (C═O) and edge defects, were suggested to present a high redox potential to facilitate electron transfer to PMS to generate free radicals. In a subsequent study, the rGO activated with CO_2 demonstrated a high specific surface area (SSA > 1200 m^2/g) and an enhanced activity toward PMS activation.[2] Similar to PMS, the essence of PS activation depends on the abilities of breaking-up of SO-OS bond and conducting the electron transfer from catalysts or organic compounds to PS.

In this study, for the first time, we observed that nanocarbons such as SWCNTs, rGO-900, and CMK-8 have superb catalytic activities to activate PS for phenol oxidation. However, C_{60}, g-C_3N_4, and nanodiamond presented poor performances. SWCNTs and MWCNTs are composed of highly sp^2-hybridized graphitic carbon structure with low defects and oxygen levels, confirming that the abundant free-flowing π electrons might be effective to activate PS to form reactive radicals. Additionally, the bent graphene sheets of CNTs contained partially delocalized π electrons and provide better access to the reactants (PS), thus further enhancing the catalytic activity.[24] Nanodiamond possesses a sp^3-hybridized core and is coated with amorphous carbon, presenting no effectiveness for PS activation. However, CMK-8 (amorphous carbon) with high oxygen contents and defective degrees (I_D/I_G = 1.49) demonstrates great performance for phenol oxidation, suggesting that the defective edges and oxygen groups can be active sites. This is further supported by the catalysis on chemically derived rGO-900, which has a sp^2 carbon lattice and the highest defective degrees (I_D/I_G = 1.70) with plentiful zigzag edges, vacancy defects, nonhexagonal units, and functional groups formed during the thermal annealing, and demonstrates the best performance for PS activation. Additionally, the porous structure of nanocarbons, which possess large pore volume and high specific surface area, not only facilitates the adsorption of phenol and enhances mass transfer process but also provides more exposed active sites for surface catalytic reactions. To further probe the effective species, three kinds of small molecular catalysts (benzoquinone, 1,4-dicarboxybenzene, and 1,2-dihydroxybenzene) were employed to mimic different oxygen groups of carbonyl groups (C═O), carboxyl groups (−COOH), and hydroxyl groups (−OH) respectively.[33,34] The *in situ* electron paramagnetic resonance (EPR) spectra in Figure 5 and Figure S10 (SI) revealed that the carbonyl presented the strongest intensities and demonstrated much better performance to activate PS for reactive radical generation, suggesting C═O is the main active sites among the oxygen groups. It is interesting to note that graphene oxide possesses high oxygen contents (over 30 at. %), yet demonstrates very poor activity toward phenol adsorption and PS activation (Figure S11, SI). The catalytic activity was dramatically enhanced after removing most of the oxygen groups via thermal annealing (rGO-900). The same phenomenon was also observed in our previous study for PMS activation.[19] As the electron transfer process is influenced by the relative electronic potential between the carbocatalysts and persulfate, the excess of oxygen contents will significantly affect the reducibility of graphene, which is not beneficial for the electron transfer from graphene to PMS or PS. Thus, for future design of efficient carbocatalysts, both the oxygen level and species of oxygen groups should be optimized. The experimental results suggest that the relationship between dimension effect and catalytic performance is poor. The catalytic activity of nanocarbons for PS activation indeed origins from the carbon-conjugated structure, defective sites, and proper amounts of functional groups.

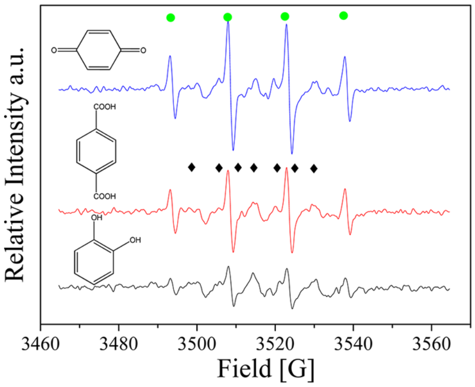

Figure 5. EPR spectra of PS activation on (a) benzoquinone, (b) 1,4-dicarboxybenzene, and (c) 1,2-dihydroxybenzene. (●: DMPO−OH, ◆: DMPO−SO_4) [Temp] = 25 °C; [PS] = 6.5 mM; [Catalyst] = 20 ppm; [DMPO] = 0.08 M.

Classic metal (Fe^0) and metal oxides (Fe_3O_4, CuO, Co_3O_4, and MnO_2) were employed to compare with the metal-free catalysts. Figure 6 indicates that Fe_3O_4, CuO, and Co_3O_4 presented poor catalytic activities, leading to 16.4%, 22.3%, and 29.1% phenol oxidation, respectively. MnO_2 was able to effectively activate PS with 92.0% phenol degradation in 180 min. The zerovalent iron (ZVI) worked as electron donors to stimulate PS ($S_2O_8^{2-}$) to generate sulfate radicals ($SO_4^{\bullet-}$), providing 100% phenol removal in 30 min. However, it can be seen that nanocarbons, such as MWCNTs, SWCNTs, and CMK-8, are more effective than most of the metal oxides for PS activation. rGO-900 was even comparable to the most efficient metal catalyst, ZVI, meanwhile completely removing the introduction of metal ions (Fe^{3+}) to the water body.

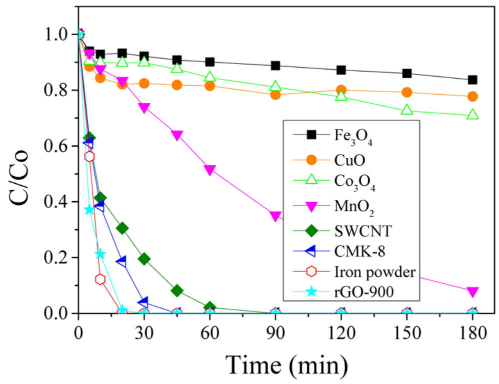

Figure 6. Comparison of metal and metal-free catalysts for PS activation. [Catalyst] = 0.2 g/L; [Temp] = 25 °C; [PS] = 6.5 mM; [Phenol] = 20 ppm.

The stability tests of rGO-900, SWCNTs, and CMK-8 were performed and shown in Figure 7. Fresh rGO-900 could completely decompose 20 ppm phenol in just 30 min, and 81.2% and 57.7% of phenol removals were achieved in 180 min, respectively, in the second and third runs. SWCNTs provided 100% phenol oxidation in the first run, and 85.2% and 70.7% for the second and third cycles. CMK-8 was able to obtain 100%, 94.9%, and 61.3% of phenol decomposition for the three cycles. Yang et al. found that activated carbon could catalyze

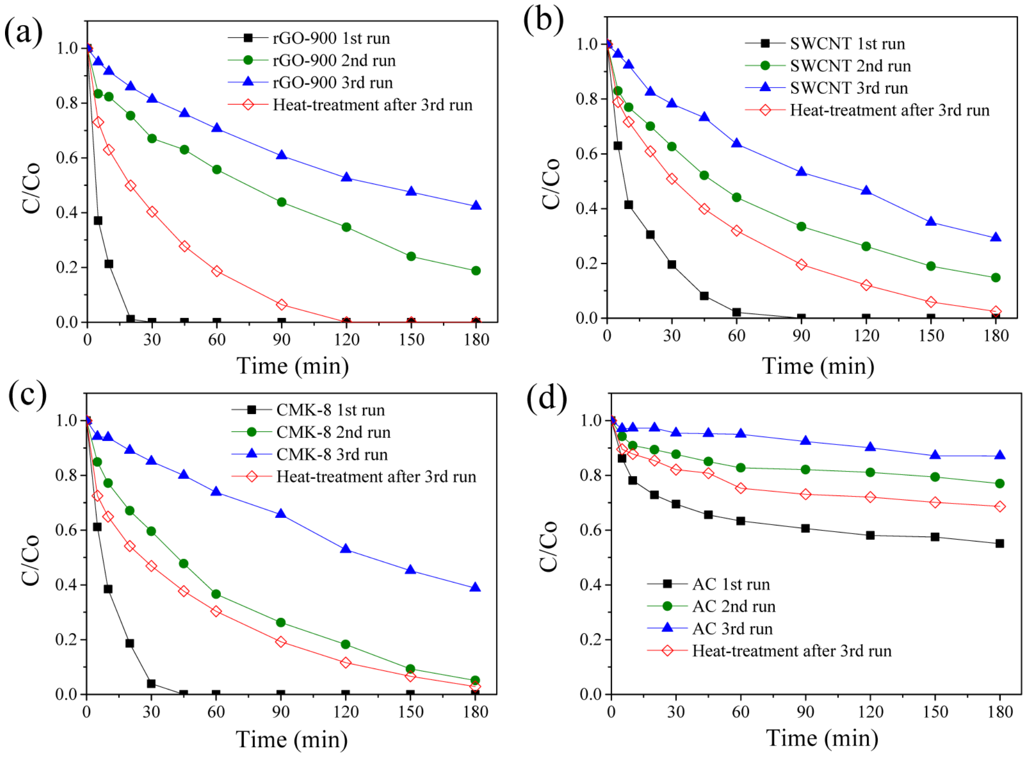

Figure 7. Stability and regeneration tests of (a) rGO-900, (b) SWCNTs, (c) CMK-8, and (d) activated carbon. [Catalyst] = 0.2 g/L; [Temp] = 25 °C; [PS] = 6.5 mM; [Phenol] = 20 ppm.

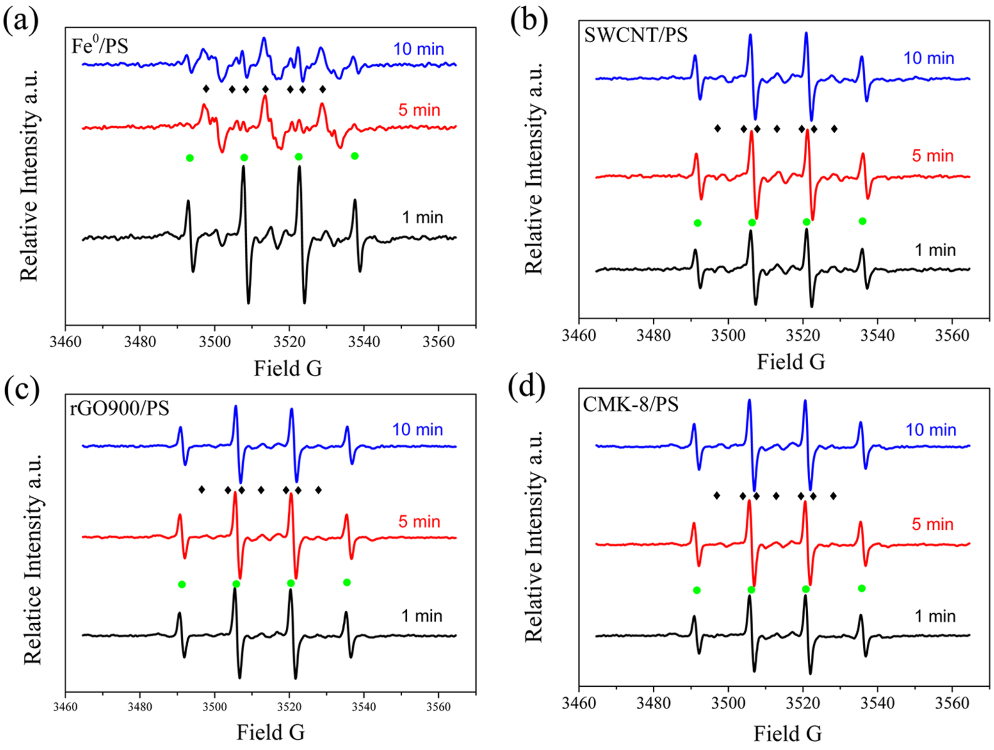

Figure 8. EPR spectra of (a) rGO-900, (b) SWCNTs, (c) CMK-8, and (d) activated carbon. (●: DMPO−OH, ◆: DMPO−SO_4) [Catalyst] = 0.2 g/L; [Temp] = 25 °C; [PS] = 6.5 mM; [Phenol] = 20 ppm; [DMPO] = 0.08 M.

persulfate to degrade dyes.[35] An activated carbon (SSAs 821.3 m^2/g, pore volume 0.011 cm^3/g) was then tested, which provides 44.9%, 23.0%, and 12.9% phenol removal for the first, second, and third runs, respectively. It is well reported that the deactivation of metal oxides in heterogeneous catalysis was mainly due to changes of surface crystal structure and coverage of intermediates. In terms of ZVI, the surface of ZVI was quickly covered and wrapped by ferric hydroxide or ferrous sulfate in the activation of PS, thus preventing the further interaction of ZVI and PS.[36] However, the passivation of nanocarbons in activation of PS is different from metals and metal oxides. Table S1 (SI) and Figure S12 (SI) suggest that the pore structure and surface chemistry of rGO-900 and SWCNTs changed significantly after the first run, due to the reconstruction of carbon structure and coverage of phenol and organic intermediates, which presented strong interaction with the sp^2 hybridized carbon system. Interestingly, it can be seen that SWCNTs presented a better reusability than the chemically derived rGO, which was possibly ascribed to the more stable and highly graphitic shell structure.[37] The activated carbon possesses much larger SSAs than rGO-900 and SWCNTs and smaller pore volume than the CMK-8, but presenting the poorest catalytic activity and stability. At the current stage, the stability of emerging nanocarbons for AOPs might be not comparable to the commercially used metal-based catalysts used in oxidative dehydrogenation or electrochemical reactions. Nevertheless, carbon catalysts do have advantages such as a high efficiency for PS activation, a better stability than the ZVI, and the metal-free nature avoiding toxic metal leaching (iron, silver, or copper ions) to the waterbody. For carbocatalysts, the activity of deactivated catalysts could commonly be recovered by post-treatment such as thermal annealing or hydrogenation at a mild condition to remove the adsorbed intermediates and to retain the better reductive degree from oxidation in practical applications.[38−40] Therefore, the passivated carbocatalysts after the third run were reactivated via heat-treatment, and the catalytic activities were partially recovered. More specifically, regenerated rGO provided complete phenol oxidation in 120 min and 97.5%, 97.2%, and 31.4% phenol removal efficiencies were achieved on SWCNTs, CMK-8, and activated carbon in 180 min, respectively. This study presented novel ideas for green catalysis and raised a new and efficient metal-free catalytic system in activation of PS for pollutant degradation. Further investigations need to be done to improve the stability and develop efficient and robust metal-free catalysts in future applications.

Electron paramagnetic resonance was utilized as a powerful tool to probe the PS activation and radical revolution processes on nanocarbons. A classical spin-trapping agent, 5, 5-dimethylpyrroline-oxide (DMPO), was used to capture the free radicals during the PS activation. Interestingly, we discovered that ZVI was able to activate PS to generate large amounts of hydroxyl radicals in the first 1 min and subsequently generated sulfate radicals in 5 and 10 min (see Figure 8a). It has been well reported in many studies that iron ions mainly activated persulfate to generate sulfate radicals eq 1,[14−17] which suggests that the PS activation on ZVI is different from that in Fe^{2+}/PS systems. As PS itself can hardly produce hydroxyl radicals, and intertransfer between $SO_4^{\bullet -}$ to $^{\bullet}OH$ only contributes to very small amounts of hydroxyl radicals; most of the hydroxyl radicals can be only originated from the water. ZVI might be able to directly activate PS by oxidizing water via a four-electron pathway, and ZVI itself works as the electron donor as well eq 2. We suggest that the mechanisms of heterogeneous and homogeneous activations of persulfate are different. This is further verified by the nanocarbons catalysis, which preferably produce hydroxyl radicals $^{\bullet}OH$. It is indicated in Figure 8b−d that large amounts of $^{\bullet}OH$ and small portion of $SO_4^{\bullet -}$ were generated in the SWCNT/PS, rGO-900/PS and CMK-8/PS systems throughout the reaction. Because sulfate radicals possesses higher oxidative potential (2.5−3.1 V) than hydroxyl radicals (2.7 V), the O−O bond of persulfate is first activated and weakened on the active sites of carbocatalysts, following by directly oxidizing the adsorbed water or hydroxyl groups (OH^-) to generate hydroxyl radicals via one-step process. The mechanism of PS activation on carbocatalysts was illustrated in Scheme 1. It is suggested that the carbon matrix (similar to ZVI) can also work as an excellent electron bridge to facilitate the fast electron-transfer processes. Therefore, nanocarbons with various kinds of active sites and networks present different capabilities for PS activation, water, and phenol adsorption, and electron transfer, thus presenting different performances in PS activation and phenol oxidation. It is also worthwhile noting that, different from metal-based systems, the highly covalent carbon network might play a crucial role to interact and activate the benzene ring of the organic matters, which helps the ring-open processes and synergistically promotes the attack and oxidation by the reactive radicals.

Scheme 1. Proposed Mechanism of PS Activation on Carbocatalysts

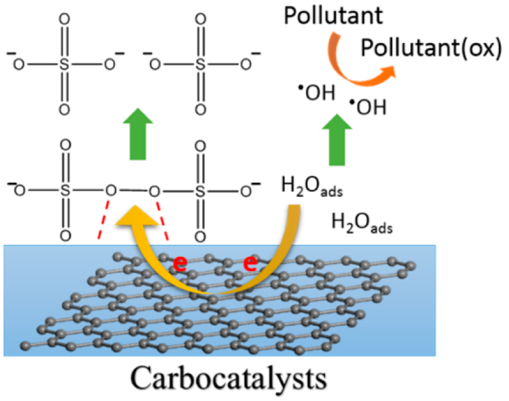

$$S_2O_8^{2-} + Fe^{2+} \rightarrow SO_4^{\bullet -} + Fe^{3+} \qquad (1)$$

$$S_2O_8^{2-} + Fe^{0} + 2H_2O \rightarrow 2SO_4^{2-} + Fe^{2+} + 2^{\bullet}OH + 2H^{+} \qquad (2)$$

CONCLUSIONS

In this study, various nanocarbons were tested as metal-free catalysts for catalytic oxidation of organic contaminants. For the first time, we found that SWCNTs, reduced graphene oxide, and CMK-8 demonstrated superior efficiencies for PS activation, whereas C_{60}, g-C_3N_4 and nanodiamond presented poor activity. The carbocatalysts showed much higher activity than the universally used metal oxides such as Fe_3O_4, CuO, Co_3O_4, and MnO_2. In addition, rGO-900 was even comparable to the most efficient electron donor of ZVI. Meanwhile nanocarbons as catalysts completely avoid the metal leaching problems into the water body. Both the characterization and adsorption/oxidation results revealed that the dimension might affect the phenol adsorption capability, while catalytic activity of nanocarbons is strongly dependent on the conjugation of carbon network, defective sites, and proper amounts of functional groups (especially the carbonyl groups). More importantly, this is the first mechanistic study on PS activation on nanocarbons. The EPR results revealed that heterogeneous activation of PS is different from homogeneous systems and carbocatalysts can effectively activate PS molecules via directly oxidizing adsorbed water through the carbon bridge. Future study is still required to envisage further insights into the relationship between each active site and its capability toward PS activation, water adsorption, and charge transfer processes. This study not only reports several green catalysts for PS activation but also contributes to exploring new advanced oxidative systems for wastewater treatment without secondary contamination. It is also inspiring to note that, as hydrogen peroxide is more difficult to be activated on heterogeneous catalysts (especially for nanocarbons) to generate hydroxyl radicals, this study might open up a brand new way using the metal-free catalysis for hydrogen peroxide-based systems such as Fenton reaction, photocatalysis, electrochemistry, and versatile selective oxidation processes.

■ EXPERIMENTAL SECTION

Chemicals and Materials. Potassium peroxydisulfate (PS, >99.0%), melamine (>99.0%), diamond nanopowder (>97.0%, <10 nm), and 5,5-dimethylpyrroline-oxide (DMPO, >99.0%) were purchased from Sigma-Aldrich. Phenol (>99.0%), 2,4-dichlorophenol (2,4-DCP, >99.0%), methylene blue (>99.0%), and methanol (absolute) were obtained from Chem-Supply. Fullerene (C_{60}, >99.5%) and 3D cubic-ordered mesoporous carbon (CMK-8, >99.6%) were purchased from XF Nano, Nanjing, China. The single-walled carbon nanotubes (SWCNTs) and multiwalled carbon nanotubes (MWCNTs) were obtained from Timesnano, Chengdu, China. Activated carbon (AC) was purchased from Picactive Co. Ltd., Indonesia. All carbon materials were used as received.

Synthesis of Reduced Graphene Oxide, g-C_3N_4 and Metal Oxides. Graphene oxide (GO) was synthesized via a modified Hummers' method as reported in our previous studies.[2,19] To prepare the reduced graphene oxide (rGO), GO was ground finely and transferred to a quartz boat placed in a tubular furnace. Nitrogen was applied as the protection gas with a flow rate of 50 mL/min. After the quartz tube was purged by N_2 flow for 2 h, the temperature was elevated to 450 °C for 1 h with a heating rate of 5 °C/min to make GO fully expanded. The temperature was then raised to 900 °C and kept for 1 h to remove the oxygen groups and cooled to room temperature naturally. The fluffy black powder was washed with water and ethanol several times and dried in an oven overnight at 60 °C. Thus, rGO was obtained and denoted as rGO-900. Graphitic carbon nitride (g-C_3N_4) was prepared by a one-pot thermal condensation method. Briefly, melamine (5.0 g) was placed in a crucible with a lid and transferred to a muffle furnace under static air atmosphere, annealing with a heating rate of 5 °C/min and kept at 550 °C for 2 h, then cooling naturally. A yellow product was ground finely and collected for use. Preparation procedures of referenced metal oxides of Fe_3O_4, CuO, Co_3O_4, and MnO_2 can be found in Supporting Information.

Characterization of Materials. Nitrogen sorption isotherms were acquired from a Tristar 3000 at −196 °C to evaluate the Brunauer−Emmett−Teller (BET) specific surface area. Porous structure and pore size distribution were estimated by the Barrett−Joiner−Halenda (BJH) method (desorption). Raman spectra were studied on an ISA dispersive argon laser Raman spectrometer (514 nm). The surface elemental information was obtained from X-ray photoelectron microscopy (XPS, Thermo Escalab 250) under Al Kα X-ray. The XPS spectra were fitted with CasaXPS software, calibrated to the binding energy of primary C 1s peak at 284.5 eV. The chemical component fitting applied the Voigt functions with the Shirley background and a 30% Lorentzian component.

Catalytic Activity Tests. The adsorption and catalytically oxidative degradation of phenol were carried out in a batch reactor. At each time interval, the reaction solution was withdrawn, filtered and injected into a vial. In catalytic oxidation, 0.5 mL of methanol as a radical scavenger was immediately injected to the vial to quench the oxidation reaction. The sample was analyzed by an UltiMate 3000 ultrahigh performance liquid chromatography plus (UHPLC$^+$) from Thermo-Fisher Scientific for monitoring phenol concentration and intermediates with UV lamp at 270 nm with a C18 column. The mobile phase was made of 30 wt % acetonitrile and 70 wt % ultrapure water at a flow rate of 1 mL/min. After each run, the carbocatalysts were recycled, washed by water and ethanol several times, and dried in an oven at 60 °C overnight for reuse. 2,4-DCP, catechol, and 1,4-dihydroxybenzene were also tested using the similar protocols. Methylene blue was degraded and monitored by UV−visible spectroscopy. After each run, the carbocatalysts were collected and washed with ethanol and ultrapure water several times, and then dried in an oven at 60 °C overnight for reuse. The passivated catalysts after the third run was regenerated via thermal treatment. Briefly, the catalysts was first washed and dried, then annealed in a muffle furnace (statistic atmosphere) at 350 °C for 1 h with a heating rate of 5 °C/min and cooled naturally.

Mechanism Study of Radical Evolution. An EMS-plus electron paramagnetic resonance (Bruker, Germany) was utilized to capture the generated active radicals with a spin trapping agent of 5,5-dimethylpyrroline-oxide. The instrument was operated in following conditions: Centre field: 3514.7 G; sweep width: 100 G; microwave frequency: 10.0 GHz; power setting: 18.88 mW; scan time: 30 s; scan number: 2. The EPR spectra were analyzed and exported by Bruker Xeon software. The DMPO radical adducts were identified by hyperfine splitting constants of DMPO−OH (α_N = 14.8, α_H = 14.8) and DMPO−SO_4 (α_N = 13.2, α_H = 9.6, α_H =1.48, and α_H =0.78).

■ ASSOCIATED CONTENT

Ⓢ Supporting Information

The Supporting Information is available free of charge on the ACS Publications website at DOI: 10.1021/acscatal.5b00774.

> Synthesis procedure of metal oxides, XPS spectra, adsorption tests, and evaluation of intermediates (PDF)

■ AUTHOR INFORMATION

Corresponding Authors

* (S.W.) E-mail: shaobin.wang@curtin.edu.au. Phone: +61 8 9266 3776.
* (H.S.) E-mail: h.sun@curtin.edu.au. Phone: +61 8 9266 5403.

Notes

The authors declare no competing financial interest.

■ ACKNOWLEDGMENTS

This work was financially supported by Australian Research Council (ARC DP130101319). H.S. appreciates the support from Curtin Research Fellowship.

■ REFERENCES

(1) Shukla, P. R.; Wang, S. B.; Sun, H. Q.; Ang, H. M.; Tade, M. O. *Appl. Catal., B* **2010**, *100*, 529−534.

(2) Peng, W. C.; Liu, S. Z.; Sun, H. Q.; Yao, Y. J.; Zhi, L. J.; Wang, S. B. *J. Mater. Chem. A* **2013**, *1*, 5854−5859.

(3) Liu, S. Z.; Peng, W. C.; Sun, H. Q.; Wang, S. B. *Nanoscale* **2014**, *6*, 766−771.
(4) Hussain, H.; Green, I. R.; Ahmed, I. *Chem. Rev.* **2013**, *113*, 3329−3371.
(5) Zhang, T.; Chen, Y.; Wang, Y.; Le Roux, J.; Yang, Y.; Croué, J. P. *Environ. Sci. Technol.* **2014**, *48*, 5868−5875.
(6) Kolthoff, I. M.; Miller, I. K. *J. Am. Chem. Soc.* **1951**, *73*, 3055−3059.
(7) Yang, S. Y.; Wang, P.; Yang, X.; Shan, L.; Zhang, W. Y.; Shao, X. T.; Niu, R. *J. Hazard. Mater.* **2010**, *179*, 552−558.
(8) Yang, Y.; Pignatello, J. J.; Ma, J.; Mitch, W. A. *Environ. Sci. Technol.* **2014**, *48*, 2344−2351.
(9) Kronholm, J.; Metsala, H.; Hartonen, K.; Riekkola, M. L. *Environ. Sci. Technol.* **2001**, *35*, 3247−3251.
(10) Kronholm, J.; Riekkola, M. L. *Environ. Sci. Technol.* **1999**, *33*, 2095−2099.
(11) Furman, O. S.; Teel, A. L.; Watts, R. J. *Environ. Sci. Technol.* **2010**, *44*, 6423−6428.
(12) Ahmad, M.; Teel, A. L.; Watts, R. J. *Environ. Sci. Technol.* **2013**, *47*, 5864−5871.
(13) Fang, G. D.; Gao, J.; Dionysiou, D. D.; Liu, C.; Zhou, D. M. *Environ. Sci. Technol.* **2013**, *47*, 4605−4611.
(14) Cai, C.; Zhang, H.; Zhong, X.; Hou, L. *Water Res.* **2014**, *66*, 473−485.
(15) Chen, L. C.; Zeng, X. T.; Si, P.; Chen, Y. M.; Chi, Y. W.; Kim, D. H.; Chen, G. N. *Anal. Chem.* **2014**, *86*, 4188−4195.
(16) Drzewicz, P.; Perez-Estrada, L.; Alpatova, A.; Martin, J. W.; El-Din, M. G. *Environ. Sci. Technol.* **2012**, *46*, 8984−8991.
(17) Ahn, S.; Peterson, T. D.; Righter, J.; Miles, D. M.; Tratnyek, P. G. *Environ. Sci. Technol.* **2013**, *47*, 11717−11725.
(18) Anderson, J. M.; Kochi, J. K. *J. Am. Chem. Soc.* **1970**, *92*, 1651−1659.
(19) Sun, H. Q.; Liu, S. Z.; Zhou, G. L.; Ang, H. M.; Tade, M. O.; Wang, S. B. *ACS Appl. Mater. Interfaces* **2012**, *4*, 5466−5471.
(20) Lee, H.; Lee, H. J.; Jeong, J.; Lee, J.; Park, N. B.; Lee, C. *Chem. Eng. J.* **2015**, *266*, 28−33.
(21) Sun, H. Q.; Kwan, C.; Suvorova, A.; Ang, H. M.; Tade, M. O.; Wang, S. B. *Appl. Catal., B* **2014**, *154*, 134−141.
(22) Yu, Z.; Tetard, L.; Zhai, L.; Thomas, J. *Energy Environ. Sci.* **2015**, *8*, 702−730.
(23) Zhi, M. J.; Xiang, C. C.; Li, J. T.; Li, M.; Wu, N. Q. *Nanoscale* **2013**, *5*, 72−88.
(24) Zhang, J. A.; Su, D. S.; Blume, R.; Schlogl, R.; Wang, R.; Yang, X. G.; Gajovic, A. *Angew. Chem., Int. Ed.* **2010**, *49*, 8640−8644.
(25) Wu, S.; Wen, G.; Wang, J.; Rong, J.; Zong, B.; Schlogl, R.; Su, D. S. *Catal. Sci. Technol.* **2014**, *4*, 4183−4187.
(26) Chen, P. R.; Chew, L. M.; Xia, W. *J. Catal.* **2013**, *307*, 84−93.
(27) Buchwald, S. L.; Bolm, C. *Angew. Chem., Int. Ed.* **2009**, *48*, 5586−5587.
(28) Banks, C. E.; Crossley, A.; Salter, C.; Wilkins, S. J. *Angew. Chem., Int. Ed.* **2006**, *45*, 2533−2537.
(29) Zhang, J.; Comotti, M.; Schuth, F.; Schlogl, R.; Su, D. S. *Chem. Commun.* **2007**, 1916−1918.
(30) Su, C. L.; Acik, M.; Takai, K.; Lu, J.; Hao, S. J.; Zheng, Y.; Wu, P. P.; Bao, Q. L.; Enoki, T.; Chabal, Y. J.; Loh, K. P. *Nat. Commun.* **2012**, *3*, 1298.
(31) Frank, B.; Zhang, J.; Blume, R.; Schlogl, R.; Su, D. S. *Angew. Chem., Int. Ed.* **2009**, *48*, 6913−6917.
(32) Frank, B.; Blume, R.; Rinaldi, A.; Trunschke, A.; Schlogl, R. *Angew. Chem., Int. Ed.* **2011**, *50*, 10226−10230.
(33) Wu, S. C.; Wen, G. D.; Liu, X. M.; Zhong, B. W.; Su, D. S. *ChemCatChem* **2014**, *6*, 1558−1561.
(34) Wen, G. D.; Wu, S. C.; Li, B.; Dai, C. L.; Su, D. S. *Angew. Chem., Int. Ed.* **2015**, *54*, 4105−4109.
(35) Yang, S. Y.; Yang, X.; Shao, X. T.; Niu, R.; Wang, L. *J. Hazard. Mater.* **2011**, *186*, 659−666.
(36) Al-Shamsi, M. A.; Thomson, N. R. *Ind. Eng. Chem. Res.* **2013**, *52*, 13564−13571.
(37) Duan, X. G.; Sun, H. Q.; Wang, Y. X.; Kang, J.; Wang, S. B. *ACS Catal.* **2015**, *5*, 553−559.
(38) Sun, H. Q.; Wang, Y. X.; Liu, S. Z.; Ge, L.; Wang, L.; Zhu, Z. H.; Wang, S. B. *Chem. Commun.* **2013**, *49*, 9914−9916.
(39) Duan, X. G.; Ao, Z. M.; Sun, H. Q.; Indrawirawan, S.; Wang, Y. X.; Kang, J.; Liang, F. L.; Zhu, Z. H.; Wang, S. B. *ACS Appl. Mater. Interfaces* **2015**, *7*, 4169−4178.
(40) Duan, X. G.; O'Donnell, K.; Sun, H. Q.; Wang, Y. X.; Wang, S. B. *Small* **2015**, *11*, 3036.